Article ID: 1000-324X(2012)05-0550-05 **DOI:** 10.3724/SP.J.1077.2012.11743

Microstructure Characterization and Thermal Conductivity Analysis of Plasma Sprayed ZrO_2 Coatings

WANG Yong-Zhe[1], WU Wei[1], HUA Jia-Jie[1], ZENG Yi[1], ZHENG Xue-Bin[2], ZHOU Ying[3], WANG Hu[3]

(1. The State Key Lab of High Performance Ceramics and Superfine Microstructure, Shanghai Institute of Ceramics, Chinese Academy of Sciences, Shanghai 200050, China; 2. Key Laboratory of Inorganic Coating Materials, Shanghai Institute of Ceramics, Chinese Academy of Sciences, Shanghai 200050, China; 3. Shanghai Institute of Measurement and Testing Technology, Shanghai 201203, China)

Abstract: Yttria stabilized zirconia coatings were deposited using two different sets of parameters (N1, N2 coating). The microstructure features, such as total porosity and large porosity, were quantified by means of scanning electron microscope and image analysis. The three-dimensional distribution of microcracks and segmentation cracks was successfully revealed by the X-ray microscopy in the scanning electron microscope with three-dimensional microtomography capability. So the relationship between microstructure and thermal conductivity was found. At room temperature, thermal conductivity of N2 was lower than that of N1 due to larger pores and microcracks. At 1000℃ thermal conductivity of N1 was lower for the sintering of microcracks. The segmentation cracks formed by the propagation of microcracks could effectively reduce the thermal conductivity at high temperature.

Key words: ZrO_2 coatings; microstructure; thermal conductivity; X-ray microscopy

Plasma sprayed yttria-stabilized zirconia coatings continue to dominate the application of thermal barrier coatings for gas turbine engines to improve the durability and reliability as well as the efficiency of engines[1-2]. During the spray process, powder materials are injected within the plasma jet where they are accelerated and partially or totally melted, then flatten upon impact and solidify onto the substrate, forming splats. Then the coatings are built up by the layering of splats[3]. At last, this process leads to the formation of coatings with lamellar microstructure and other microstructure defects such as interlamellar pores and large globular pores. In addition, the rapid quenching associated with the plasma spray process causes microcracks with high density in the coatings[4-6]. These microstructure features, as a consequence, have a great impact on the thermal property of the coatings[7-8].

Recent investigations on plasma sprayed coatings have always focused on the relationship between microstructure and coating behavior such as thermal conductivity. Chi[9]and Kulkarni *et al*[10] demonstrated that interlamellar pores played a significant role in the reduction of thermal conductivity. Kachanov[11] and Ahmaniemi *et al*[12] reached a conclusion that horizontal cracks reduced the thermal conductivity of the coatings in the direction of heat transfer. In order to establish relationships between microstructure and thermal conductivity, the microstructure characterization is the crucial issue to solve. However, techniques widely used such as image analysis[13-15] require reliable and reproducible cross-sectional images, and small-angle neutron scattering (SANS) needed 3–4 mm thick coatings to be deposited[16]. And both of them can not yield compositional information because it is merely a two-dimensional image. Until now, there have few studies investigating the internal microstructure of the coatings, and it is difficult to obtain an all-around three-dimensional characterization of the microstructure.

In this study, the microstructure features such as total porosity and large pores were quantified by scanning electron microscope combining with image analysis. The X-ray microscopy and microtomography were used to detect the porosity and cracks within the coatings and obtain insights into the three-dimensional microstructure.

1 Experimental procedure

1.1 Materials and preparation

The commercially available fused and crushed ZrO_2-3mol%Y_2O_3 powder was used as starting material (with the medium size of 41 μm). The Metco A-2000 atmospheric plasma spray equipment with a F4-MB plasma gun (Sulzer

Received date: 2011-12-02; **Modified date:** 2012-02-10; **Published online:** 2012-02-18
Foundation item: Science and Technology Innovation Project of Shanghai Institute of Ceramics(Y17ZC5150G); Research Fund for Nanomaterials of Shanghai (11nm0506900)
Biography: WANG Yong-Zhe(1985–), male, candidate of master degree. E-mail: yongzhew@student.sic.ac.cn
Corresponding author: ZENG Yi, Professor. E-mail: zengyi@mail.sic.ac.cn

Metco AG, Switzerland) was adopted to deposit coatings. Meanwhile, the parameters of plasma spray gun were summarized in Table 1. In addition, the in-flight particle velocity and particle temperature prior to impact onto target substrate were measured using on-line monitoring system (Spray Watch 2i, OSEIR, Finland), also as shown in Table 1. Prior to spraying, the aluminum substrates were grit blasted and degreased ultrasonically in acetone.

1.2 Characterization of specimens

Free-standing coatings were used to characterize microstructure. The porosity was measured by quantitative image analysis on scanning electron microscope. The polished coatings cross-section was obtained using the standard procedures for thermal spray ceramic coatings. Vacuum impregnation was employed to prevent major pullouts in metallographic preparation. In order to measure the porosity, the back-scattered electron imaging mode was adopted for sharp contrast between pores and ceramic matrix. And fifteen fields of each specimen were selected stochastically.

The two-dimensional X-ray images were obtained by the Gatan X-ray Ultramicroscopy which was a high performance scanning electron microscopy-hosted X-ray Microscope. Au target was used with the accelerating voltage of 30 kV. The resulting average detected X-ray energy is constrained by the accelerating voltage and the detector sensitivity to around 9.7 kV. The coatings were thinned to 15–30 μm on the Gatan Centar Frontier to allow transmission of the relatively soft X-ray, then mounted and coated with 50 nm of platinum using a Gantan PECS. After imaging, a small sliver was cut from each coating to acquire tomographic datasets which consisted of 190 images of the samples with 1° interval. Each set of tomographic images was processed through phase retrieval to convert the phase-contrast images into the form suitable for the combined use with a conventional tomographic reconstruction algorithm[17]. The Gatan GPU accelerated cone beam reconstruction software in Digital Micrograph was adopted for tomographic reconstruction of the three-dimensional volume from the processed images.

Thermal diffusivity α of coatings was measured using laser flash method, and the specific heat capacity (C_p) was measured by Differential Scanning Calorimetry. Then the thermal conductivity λ was calculated by Eq.(1) where the density ρ was measured by the Archimedes method.

$$\lambda = C_p \cdot \alpha \cdot \rho \tag{1}$$

2 Results and discussion

2.1 Characterization of porosity

Figure 1(a) and (b) show the typical SEM images of polished cross-section of N1 and N2 coatings. During the image analysis, the areas which are marked with the arrows in Fig. 1 represented the large pores (one dimensional diameter is larger than 10 μm), while the rest black parts were considered to be the small pores. The total porosity was the sum of all voids, *i.e.* small pores, large pores, splats boundaries and cracks. Thus, the volume fractions of large pores and total pores of all the coatings are shown in Fig. 2.

It could be concluded that the total porosity and large porosity of N2 coating were obviously larger than that of N1 coating. The reason could be that more partially melted powders with lower particle temperature were incorporated into the coating, leading to the increase of large pores. In addition, due to lower velocity of particles, the kinetic energy of the in-flight particles was smaller, which resulted in imperfect contact of splats, increasing large pores. On the contrary, the small pores in this study could contain cracks, small voids and delamination pores, for which the measurement using image analysis was difficult.

2.2 X-ray microscopy and microtomography

Both the absorption-contrast X-ray Ultramicroscope images and the phase-contrast X-ray Ultramicroscope images of the N1 and N2 coatings are shown in Fig. 3 and Fig. 4. Absorption contrast depended on both the energy of the incident X-ray beam, the attenuating properties of structures within the sample and the thickness of those microstructures, while phase contrast arose from the

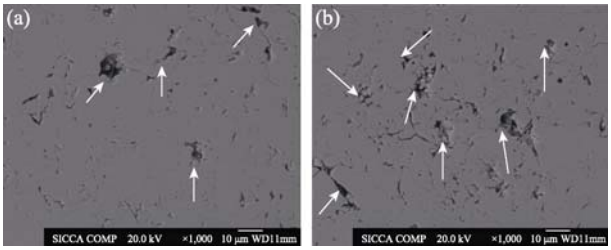

Fig. 1　SEM images of cross section of polished coatings
(a) N1; (b) N2

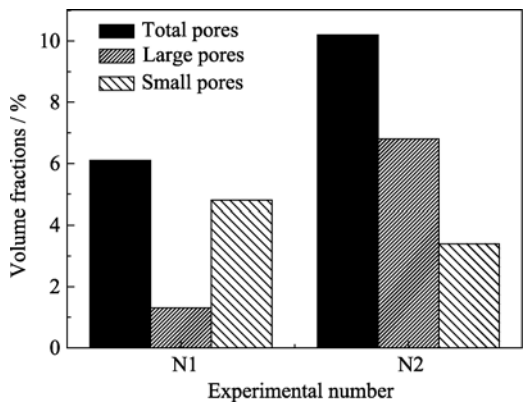

Fig. 2　Volume fractions of pores in N1 and N2 coatings

Table1 Parameters of plasma spray gun

Sample	Current/A	Ar/(L•min^{-1})	H_2/(L•min^{-1})	Spray distance/mm	Temperature/℃	Velocity/(m•s^{-1})
N1	650	35	12	120	3277	201
N2	550	35	12	120	3174	182

refraction of X-ray in samples. Large variations in refractive index could occur to samples that present very little variation in density (and hence showing little absorption contrast). The phase of X-ray passing through the samples was differentially sensitive to bulk and interfaces even though no tremendous difference is present[18]. Therefore, phase-contrast imaging could be employed to image these invisible details.

It can be clearly found that all the sprayed coatings contained microcracks in the internal microstructure (marked with the arrows in Fig. 4(b)). However, the number of microcracks are rather dependent on the spray con ditions. The N1 coating has more microcracks than the N2 coating. Microcracks were generated in the coatings as a result of the release of quenching stress as splats solidified and cooled down. With the increase of temperature, the melting state of splats would become better, which caused more microcracks after the splats solidified. In addition, the improvement of melting state of splats would lead to better bonding between the splats, which could enable the propagation of microcracks between lamellaes and the formation of through-thickness cracks. Consequently, the segmentation cracks were initiated[19]. Thus, compared with the N2 coating, there were also more segmentation cracks in the N1 coating which are marked with arrows in Fig. 3.

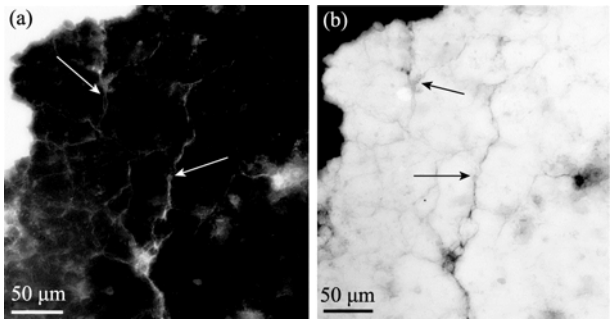

Fig. 3 X-ray microscopy images of N1 coating
(a) Absorption-contrast projection image; (b) Phase-contrast image

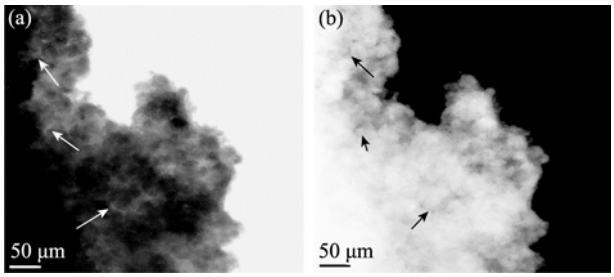

Fig. 4 X-ray microscopy images of N2 coating
(a) Absorption-contrast projection image; (b) Phase-contrast image

The reconstructed cross section of N1 coating is shown in Fig. 5, which provides a better sense of the three-dimensional distribution of the cracks. In agreement with the findings in Fig. 3, a large number of microcracks and segmentation cracks are present in N1 coating.

2.3 Thermal conductivity

The thermal conductivity of N1 and N2 coatings was measured in the temperature ranging from room temperature to 1000℃. The result is illustrated in Fig. 6.

Figure 6 shows both the thermal conductivity of N1 and N2 coatings decrease with the increase of temperature. It could be explained by the phonon (lattice waves) conduction behavior. Interaction between phonon scattering by grain boundaries and point defects, which widely existed in the coatings, resulted in the intrinsic thermal conductivity being inversely proportional to

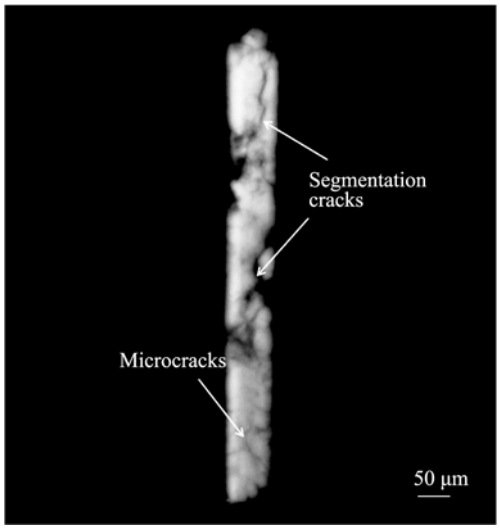

Fig. 5 Reconstructed cross section of N1 coating

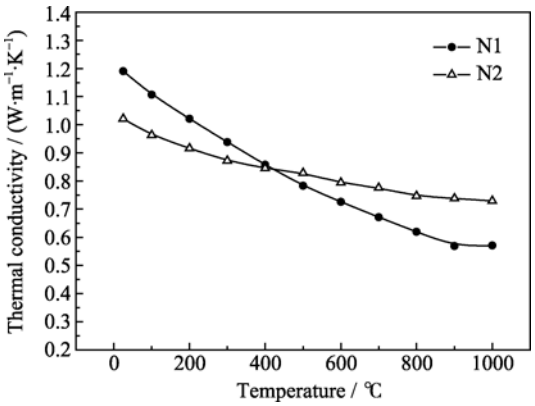

Fig. 6 Thermal conductivity of N1 and N2 coatings

temperature[20]. At room temperature, the thermal conductivity of N2 coating was lower than that of N1 coating. The reason might be that at low temperature the thermal conductivity of pores could be negligible, so the increase of total porosity would lead to serious scattering effect to the phonons, which further resulted in the decrease of thermal conductivity of coatings. However the thermal conductivity of N1 coating at 1000℃ was lower. This could be attributed to the sintering effect, in particular, the microcracks had a great propensity of sintering[21-22]. During the diffusivity measurement, the coatings were held for approximately several hours at the high temperature, which would cause the coatings to undergo localized sintering. It can be found from Fig. 4 that there are mass microcracks in N2 coating, as a result, the thermal conductivity increases. On the contrary, microcracks could propagate and penetrate into the adjacent lamellae to form the segmentation cracks in N1 coating for the better melting state of splats (as seen in Fig. 3). Therefore the sintering effect of segmentation cracks is not obvious. So the thermal conductivity of N1 coating with more segmentation is lower than N2 coating at high temperature.

3 Conclusion

Yttria stabilized zirconia coatings were deposited using two different sets of parameters. Compared with N2 coating, both the total porosity and large porosity of N1 coating was lower due to the high in-flight particle temperature associated with the better melting state. In addition, mass microcracks were clearly found in the internal structure of coatings by the X-ray microscopy and microtomography. A large number of segmentation cracks also existed in N1 coating and they were formed by the propagation of microcracks between splats due to higher tensile stresses during cooling. The thermal conductivity of N2 coating was lower than that of N1 coating at room temperature for strong scattering of phonons caused by higher porosity and more microcracks. At high temperature, the microcracks underwent localized sinter, however the sintering effects of segmentation cracks were not obvious. Consequently, the thermal conductivity of N1 coating was much lower.

References:

[1] Padture N P, Gell M, Jordan E H. Materials science - thermal barrier coatings for gas-turbine engine apptications. *Science,* 2002, **296(5566):** 280–284.

[2] Mauer G, Vassen R. Current developments and challenges in thermal barrier coatings. *Surf. Eng.,* 2011, **27(7):** 477–479.

[3] Hsiao W T, Su C Y, Huang T S, *et al*. The microstructural characteristics and mechanical properties of Ni-Al/h-BN coatings deposited using plasma spraying. *J. Alloys Compd.,* 2011, **509(32):** 8239–8245.

[4] Basu S N, Ye G, Gevelber M, *et al*. Microcrack formation in plasma sprayed thermal barrier coatings. *J. Refra. Meta. Mater.,* 2005, **23(4/5/6):** 335–343.

[5] Tan Y, Longtin J P, Sampath S, *et al*. Effect of the starting microstructure on the thermal properties of as-sprayed and thermally exposed plasma-sprayed YSZ coatings. *J. Am. Ceram. Soc.*, 2009, **92(3):** 710–716.

[6] Xue M, Chandra S, Mostag J, *et al*. Formation of pores in thermal spray coatings due to incomplete filling of crevices in patterned surfaces. *Plasma Chem. Plasma Process*, 2007, **27(5):** 647–657.

[7] Vourlias G, Pistofidis N, Psyllaki P, *et al*. Plasma-sprayed YSZ coatings: microstructural features and resistance to molten metals. *J. Alloys Compd.,* 2009, **483(1/2):** 382–385.

[8] Jang B K, Matsubara H. Thermophysical properties of EB-PVD coatings and sintered ceramics of 4mol% Y_2O_3-stabilized zirconia. *J. Alloys Compd.,* 2006, **419(1/2):** 243–246.

[9] Chi W G, Sampath S, Wang H. Microstructure-thermal conductivity relationships for plasma-sprayed yttria-stabilized zirconia coatings. *J. Am. Ceram. Soc.,* 2008, **91(8):** 2636–2645.

[10] Kulkarni A, Wang Z, Sampath S. Comprehensive microstructural characterization and predictive property modeling of plasma-sprayed zirconia coatings. *Acta Mater.,* 2003, **51(9):** 2457–2475.

[11] Sevostianov I, Gorbatikh L, Kachanov M. Recovery of information on the microstructure of porous/microcracked materials from the effective elastic/conductive properties. *Mater. Sci. Eng*., 2001, **318(1/2):** 1–14.

[12] Ahmaniemi S, Vuoristo P, Mantyla T, *et al*. Modified thick thermal barrier coatings: Thermophysical characterization. *J. Eur. Ceram. Soc*., 2004, **24(9):** 2669–2679.

[13] Bertrand G, Bertrand P, Roy P, *et al*. Low conductivity plasma sprayed thermal barrier coating using hollow psz spheres: correlation between thermophysical properties and microstructure. *Surf. Coat. Tech.*, 2008, **202(10):** 1994–2001.

[14] Du H, Lee S W, Shin J H. Study on porosity of plasma-sprayed coatings by digital image analysis method. *J. Therm. Spray Tech.*,

2005, **14(4):** 453–461.

[15] Wang Z, Kulkarni A, Ddeshpande S, *et al*. Effects of pores and interfaces on effective properties of plasma sprayed zirconia coatings. *Acta Mater.,* 2003, **51(18):** 5319–5334.

[16] Saruhan B, Ryukhtin V, Kelm K. Correlation of thermal conductivity changes with anisotropic nano-pores of EB-PVD deposited FYSZ-coatings. *Surf. Coat. Tech.*, 2011, **205(23/24):** 5369–5378.

[17] Mayo S C, Miller P R, Wilkins S W. Quantitative X-ray projection microscopy: phase-contrast and multi-spectral imaging. *J. Microscopy-Oxford*, 2002, **207(2):** 79-96.

[18] Zahiri S H, Mayo S C, Jahedi M. Characterization of cold spray titanium deposits by X-ray microscopy and microtomography. *Microscopy and Microanalysis*, 2008, **14(3):** 260–266.

[19] Guo H B, Vaben R, Stover D. Atmospheric plasma sprayed thick thermal barrier coatings with high segmentation crack density. *Surf. Coat. Tech.*, 2004, **186(3):** 353–363.

[20] Taylor R E. Thermal conductivity determinations of thermal barrier coatings. *Mater. Sci.Eng.,* 1998, **245(2):** 160–167.

[21] Cernuschi F, Ahmaniemi S, Vuoristo P, *et al*. Modelling of thermal conductivity of porous materials: application to thick thermal barrier coatings. *J. Eur. Ceram. Soc.*, 2004, **24(9):** 2657–2667.

等离子喷涂 ZrO_2 涂层显微结构表征和热导率分析

王墉哲[1], 吴 伟[1], 华佳捷[1], 曾 毅[1], 郑学斌[2], 周 莹[3], 王 虎[3]

(1. 中国科学院 上海硅酸盐研究所, 高性能陶瓷和超微结构国家重点实验室, 上海 200050; 2. 中国科学院 上海硅酸盐研究所, 特种无机涂层重点实验室, 上海 200050; 3. 上海市计量测试研究院, 上海 201203)

摘 要: 利用大气等离子喷涂制备了 ZrO_2 涂层, 采用扫描电子显微镜结合图像分析的方法对涂层的显微结构特征(总气孔率和大气率)进行了量化表征. 同时利用扫描电子显微镜附带 X 射线扫描成像对涂层内部的微裂纹和大的分隔裂纹的三维分布进行了表征. 据此建立了 ZrO_2 涂层显微结构与热导率之间的关系. 室温下, 涂层 N2 的热导率较 N1 的低, 因为涂层 N2 内气孔和微裂纹数较多; 在 1000℃, 由于微裂纹的烧结作用导致热导率增大, 所以涂层 N2 的热导率较 N1 反而高. 高温下, 涂层内由微裂纹汇聚而形成的大的分隔裂纹的存在则可以有效地抑制烧结, 降低涂层的热导率.

关 键 词: ZrO_2 涂层; 显微结构; 热导率; X 射线显微术

中图分类号: TQ174 **文献标识码:** A